



First-principles study of interfacial boundaries in Ni–Ni₃Al

C. Woodward^{a,*}, A. van de Walle^b, M. Asta^c, D.R. Trinkle^d

^a Materials and Manufacturing Directorate, Air Force Research Laboratory, Wright Patterson Air Force Base, Dayton, OH 45433-7817, USA

^b School of Engineering, Brown University, Providence, RI 02912, USA

^c Department of Materials Science and Engineering, University of California, Berkeley, CA 94720-1760, USA

^d Department of Materials Science and Engineering, University of Illinois, Urbana, IL 61801, USA

Received 21 January 2014; received in revised form 23 April 2014; accepted 24 April 2014

Available online 29 May 2014

Abstract

The width and energy of low-index interfacial boundaries (IFBs) in *Ni–Ni₃Al* are calculated using first-principles methods for temperatures ranging from 0 to 1300 K. The low-temperature, coherent and chemically sharp (100), (110) and (111) IFBs are studied using conventional spin-polarized density functional methods. Cluster expansion methods, as implemented in the ATAT software suite, are used to estimate the interfacial excess free energies (IEFEs) and composition and long-range order profiles of these defects as a function of temperature. The simple face-centered cubic-based cluster expansion produces interfacial widths in the range of 1.5–3.0 nm at 1000 K. Interfacial widths double in size with an increase in temperature of 500 K. We also find that the IEFEs for the (100), (110) and (111) IFBs are strongly temperature dependent, decreasing by 90% as temperature increases from 0 to 1000 K. While vibrational and electronic entropic contributions were also considered, changes in free energy are dominated by the configurational entropy. The predicted high-temperature IEFE is approximately 10 mJ m⁻² which is in excellent agreement with previous fits to experimentally measured coarsening rates.

Published by Elsevier Ltd. on behalf of Acta Materialia Inc.

Keywords: Ab initio calculations; Interfaces; Interfacial free energy; Temperature dependence; Superalloys

1. Introduction

The Ni-based superalloys have been integral to the success of high-performance turbine engines used in aerospace propulsion and terrestrial power generation. The high-temperature properties of these alloys reflect the contributions of a combination of precipitation and solid-solution strengthening mechanisms. The properties of commercial superalloys are generally adjusted through a series of heat treatments designed to produce an optimal precipitate microstructure. These microstructures consist of a face-centered cubic (fcc) Ni solid-solution matrix (γ) and a

distribution of $L1_2$ (γ') precipitates with a volume fraction ranging from 40% to 80% depending on the process route and intended application. The mechanisms thought to influence work hardening and strengthening are controlled in part by the nature of the interfacial boundary (IFB) between the solid-solution Ni matrix and the ordered-intermetallic *Ni₃Al* precipitate. The deformation (i.e. yield stress, creep, fatigue) of these alloys is strongly influenced by the manner in which dislocations interact with the precipitates and the channels between them. In order to model the dislocation–precipitate evolution it is important to have a detailed understanding of the nature of the γ – γ' interface over a wide range of temperatures. A precise microstructural evolution method, one that could predict the size distribution and spatial correlation of precipitates during non-isothermal processing, would be of great value to the superalloy community. Models of microstructure

* Corresponding author.

E-mail addresses: christopher.woodward@us.af.mil (C. Woodward), axelvandewalle@brown.edu (A. van de Walle), mdasta@berkeley.edu (M. Asta), dtrinkle@illinois.edu (D.R. Trinkle).

evolution, such as the phase-field method, are dependent on the availability of reliable kinetic as well as bulk and interfacial thermodynamics data. This includes the interfacial width and free energies over the composition and temperature range of interest.

The primary method for estimating IFB energies is based on the measurement of γ' coarsening rates. The average interfacial energy over the precipitate surface is estimated by applying the Lifshitz, Slyozov and Wanger (LSW) theory of Ostwald ripening [1,2] and extensions thereof. The experimental technique is difficult as accurate measurements of average particle size over time is challenging. Using this technique early work by various groups estimated the interfacial energy (σ) as ranging from 19 to 6 mJ m⁻² for aging temperatures ranging from 773 to 1073 K, respectively [3–6]. In addition, the coarsening model is not well suited for concentrated solid solutions interacting with an intermetallic precipitate [7]. Calderon et al. [7] extended LSW theory to incorporate both a modified Gibbs–Thomson equation to include the effects of non-ideal solution thermodynamics and the effects of solute solubility in each phase on the flux conservation condition near the interface. The new analysis produced corrected interfacial energies ranging from 42 to 80 mJ m⁻² for temperatures ranging from 848 to 863 K. This advance also led Ardell to reassess existing coarsening measurements in the mid-1990s, producing σ values ranging from 8.7 to 0.9 mJ m⁻² for temperatures from 823 to 973 K [8].

There is significant scatter in the measured values of σ and the result is strongly dependent on what model is used to describe the particle size distribution [7]. Further, recent calculations employing an atomistic scheme have demonstrated that at high temperatures the IFB spreads over a wider region and roughens [9]. Ardell and Ozolins [10] have proposed that in this case the rate limiting process for coarsening is the diffusion rate through the diffuse IFB. This implies that coarsening rates will not have the classical $t^{1/3}$ dependence but instead will exhibit a $t^{1/2}$ dependence. The new interpretation of coarsening rates produces σ of 20 mJ m⁻² as compared to 29 mJ m⁻² using the extended LSW theory on the same coarsening data in Ni–Al for annealing temperatures of \approx 1170 K.

Independent first-principles methods are of interest for this problem, as they provide a framework for predicting the relevant interfacial widths, roughness and free energies of the low-index IFBs. By alloying these materials the lattice mismatch between Ni and Ni₃Al can be controlled and the lattice mismatch in typical superalloys is less than 0.1%. In turbine airfoils the IFB between precipitate and the matrix phase is often considered to be coherent. Such a small misfit implies that simulation supercells without misfit dislocations provide a realistic approximation of the precipitate–matrix IFB.

In the earliest first-principles study of this class of interface Price and Cooper [11] used a full potential linearized muffin tin orbital (LMTO) method to estimate the (100)

interfacial energy in the atomistically sharp, zero-temperature limit. This study demonstrated that there were significant differences for (100)Ni/Ni₃Al interfacial energies treated in the nonmagnetic and ferromagnetic limits. Treating the interface using a spin-averaged (nonmagnetic) local density approximation (LDA) functional method, they found that the interface had a lower energy than the surrounding phases (e.g. a negative interfacial energy). This study also showed that spin-polarized LDA calculations produced positive interfacial energies in the range 50–100 mJ m⁻², thus spin-polarization was necessary to produce a stable interface between Ni and Ni₃Al. These results were independently confirmed by Wolverton and Zunger [12], who found a Ni₇Al phase that is stabilized relative to Ni and Ni₃Al in the spin-averaged approximation. The geometry of a sharp, stoichiometric interfacial-boundary produces short-range order similar to the Ni₇Al phase such that the negative value of the interfacial energy obtained in spin-averaged calculations correlates with the predicted stability of the Ni₇Al phase. Prior to Wolverton's work Schönfeld et al. attempted to form this phase by annealing a Ni-rich Ni–Al sample at 775 K for 24 h followed by a rapid quench. Subsequent diffuse neutron scattering measurements were unable to identify the presence of the Ni₇Al phase [13].

In this work we revisit the sharp interface problem using a pseudopotential plane-wave method within a spin-polarized generalized gradient approximation (S-GGA). In addition, we explore the Ni-rich part of the binary Ni–Al phase diagram using recently developed methods for estimating the entropic contributions to the alloy free energy. These methods are implemented in a software package, the Alloy Theory Automated Toolkit, which has been developed by one of the authors [14,15]. This method is used to evaluate the interfacial width and excess free energy as a function of temperature.

2. Computational methods

A combination of methods, most of which have previously been described in the literature, are used to calculate the structure and energies of IFBs. The Vienna Ab-initio Simulation Package (VASP) is used throughout this work to calculate the structural properties, the formation energy of various Ni–Al ordered phases and the energies of chemically sharp interfacial γ/γ' boundaries [16]. Spin polarization, pseudopotential and exchange correlation methods were assessed for predicting structural properties for Ni and Ni₃Al, including lattice mismatch. In general a plane-wave cutoff of 302 eV was employed with a k-point sampling density of 8-8-8 for the smaller supercells. Numerical k-space integration throughout the Brillouin zone is accomplished through a Gaussian broadening parameter of 0.2 eV. Ultrasoft pseudopotentials [17] and projected augmented wave (PAW) [18] pseudopotentials constructed using the local density approximation (LDA) [19] and the generalized gradient approximation (GGA)

[19] are used to evaluate the lattice parameters, lattice mismatch and elastic constants for Ni and Ni₃Al in order to establish the relative accuracy of the methods. Calculations for spin-polarized GGA employed the Vosko, Wilk and Nusair interpolation for the correlation part of the exchange correlation functional [16,20].

Given the variety of approximations we assume that the most accurate representation of the two-phase system is that which produces the best overall correspondence to experimental lattice constants, elastic moduli and particularly the lattice misfit. The results of these calculations are shown in Tables 1 and 2. The calculated results are systematically more accurate for these materials using the GGA, with a slightly better result for spin-polarized calculations. For calculations of the IFBs, ultrasoft pseudopotentials, within the spin-polarized GGA, produce both the lowest errors in the elastic constants and lattice misfit. This method is then used to calculate the chemically sharp, low-temperature interfacial γ/γ' boundaries for three low-index boundaries: (100), (110) and (111). Similarly these approximations are used to construct the reference configurations for the cluster expansion.

The use of a spin-polarized theory for the intended purpose of modeling high-temperature γ and γ' phases may at first seem counterintuitive. The Curie temperatures for Ni and Ni₃Al are approximately 633 and 48 K respectively [21,22]. However, the use temperatures for Ni-based superalloys can reach temperatures above 1050 K. Calorimetry data on the heat capacity of elemental Ni, as it passes through the magnetic transition temperature, indicate that it likely retains large magnetic fluctuations. Further, results of spin-resolved X-ray photoelectron spectroscopy suggest that the spin polarization within 0.075 nm of the Ni core does not change with temperatures up to 863 K (1.37T_c) [21]. These observations suggest that as the temperature increases, magnetic contributions to the enthalpy of Ni remain important even above the Curie temperature. From these observations and previous calculations we conclude

that the ferromagnetic state produces the best approximation of the Ni–Ni₃Al IFBs within the standard LDA/GGA approximations.

2.1. Low-temperature sharp interfacial boundaries

Unlike planar faults occurring in single-phase materials (i.e. stacking faults) the interfacial simulation cells include strain energy produced by the lattice mismatch between the two phases. Here we assume that the lattice mismatch is small enough so that the boundaries are coherent, with no misfit dislocations present. The strain energy needs to be accounted for in order to recover the interfacial energy. The simplest technique is to calculate the interfacial energy for increasing cell wavelengths (λ) normal to the boundary. In the low-temperature limit the supercells consist of pure Ni and stoichiometric Ni₃Al blocks, of length $\lambda/2$, stacked normal to the interface plane. The strain energy in the cells increases linearly with cell length and the strain-free interfacial energy can be recovered by extrapolating the cell energy to zero wavelength. However, this technique is not very precise, particularly when the IFB produces charge perturbations over several layers normal to the interfacial plane. Previous studies have found this approach unsuitable for producing precise γ/γ' IFB energies [11].

The second method requires calculating the energy of several strained reference cells. Here also the electronic structure, lattice positions and lattice parameters are optimized for interfacial supercells of increasing wavelength. For an interfacial cell of length λ reference Ni and Ni₃Al cells of length $\lambda/2$ are constructed that incorporate the in-plane lattice vectors (e.g. in the plane of the IFB) derived from the interfacial supercell. Next the length of these cells, normal to the boundary, are optimized while holding the in-plane lattice vectors constant. This constraint produces an excellent approximation of the strain energy produced in the interfacial cell. The interfacial energy is recovered by subtracting the energy of the two reference cells from

Table 1
Calculated and measured [37–39] lattice parameters, elastic constants (Mbar) and lattice misfit (δ) for Ni and Ni₃Al calculated using the PAW method.

PAW Metal	Property	Spin averaged		Spin polarized		Exp.
		LDA	GGA	LSDA	S-GGA	
Fcc Ni	a ₀ (nm)	0.34197	0.35150	0.34258	0.35219	0.35238
	K	1.144	1.968	1.175	1.942	1.860
	C ₁₁	3.185	2.480	3.476	2.704	2.481
	C ₁₂	2.227	1.712	2.019	1.561	1.549
	C ₄₄	1.383	1.121	1.618	1.294	1.242
	(err)	22%	5%	26%	4%	
	L1 ₂ Ni ₃ Al	a ₀ (nm)	0.34823	0.35685	0.349276	0.35699
K		2.183	1.779	2.171	1.773	1.739
C ₁₁		2.774	2.264	2.787	2.343	2.245
C ₁₂		1.888	1.537	1.863	1.488	1.486
C ₄₄		1.441	1.189	1.488	1.248	1.244
(err)		18%	0.5%	18%	1.4%	
δ		0.01814	0.01511	0.01936	0.01354	0.01218
error		49%	24%	59%	11%	

Table 2

Calculated and measured [37–39] lattice parameters, elastic constants (Mbar) and lattice misfit (δ) for *Ni* and *Ni₃Al* calculated using ultrasoft pseudopotentials.

USPP Metal	Property	Spin averaged		Spin polarized		Exp.
		LDA	GGA	LSDA	S-GGA	
Fcc Ni	a_0 (nm)	0.34294	0.35258	0.34221	0.35337	0.35238
	K	2.515	1.985	2.383	1.962	1.860
	C_{11}	3.154	2.506	3.034	2.380	2.481
	C_{12}	2.195	1.725	2.057	1.753	1.549
	C_{44}	1.358	1.057	1.363	1.253	1.242
	(err)	20%	6.8%	17%	4.6%	
L1 ₂ Ni ₃ Al	a_0 (nm)	0.34893	0.35769	0.34928	0.35784	0.35670
	K	2.163	1.777	2.159	1.787	1.739
	C_{11}	2.749	2.271	2.778	2.397	2.245
	C_{12}	1.870	1.529	1.849	1.481	1.486
	C_{44}	1.431	1.173	1.471	1.240	1.244
	(err)	17%	0.2%	18%	1.8%	
	δ	0.01731	0.01438	0.02044	0.01257	0.01218
	error	42%	18%	68%	3%	

the energy of the interfacial cell and normalizing to a standard unit area.

The lattice vectors used to construct (100), (110) and (111) IFBs are presented in Table 3. Care was taken in maintaining a constant k-point sampling density in reciprocal space as the aspect ratios of the cells change with increasing wavelength. A similar strategy was employed for the *Ni* and *Ni₃Al* cell reference calculations described in the previous paragraph.

2.2. Cluster expansion method and the Alloy Theoretic Automated Toolkit

We rely on the cluster expansion formalism [23–26], which represents the energy E of a crystalline alloy with a computationally efficient Hamiltonian taking the form of a polynomial in terms of occupation variables $\sigma_i = \pm 1$ indicating the type of atom (Al or Ni) residing on each lattice site i :

$$E = \sum_{i \neq j} J_{ij} \sigma_i \sigma_j + \sum_{i \neq j \neq k} J_{ijk} \sigma_i \sigma_j \sigma_k + \dots$$

The unknown coefficients, J_{\dots} , of this polynomial are called effective cluster interactions (ECIs) and are fit to a database of ab initio structural energies. It has been formally shown that an infinite series of this form can represent any

Table 3

Supercell geometries used to calculate the low-temperature sharp interfacial energies. Lattice vectors are in units of the lattice parameter and the scaling parameter (N) is varied in order to sample different cell wavelengths normal to the IFB. The k-point sampling is reduced with increasing wavelength in order to maintain a constant k-space sampling density.

Boundary	Lattice vectors			Scaling factor (N)
	\vec{a}	\vec{b}	\vec{c}	
(001)	$\langle 100 \rangle$	$\langle 010 \rangle$	$\langle 001 \rangle N$	2, 4, 8, 16
(110)	$\langle \bar{1}10 \rangle$	$\langle 001 \rangle$	$\langle 110 \rangle N$	2, 4, 8, 16
(111)	$\langle \bar{1}10 \rangle$	$\langle 11\bar{2} \rangle$	$\langle 111 \rangle N$	2, 4, 8, 16

configuration dependence of the energy [23]. Moreover, formal methods have been developed to determine the number of terms and the database size needed to achieve a given precision [14]. The ECIs can typically be determined from a reasonably sized database of ab initio calculations involving small-unit-cell atomic arrangements. These ECIs can then be used in a large-scale equilibrium lattice-gas Monte Carlo simulations of the coherent interface, without necessitating repeated large-scale ab initio calculations for each atomic configuration visited in a thermodynamic equilibrium. These tasks were carried out with the help of the Alloy Theoretic Automated Toolkit (ATAT) [14,15,27,28].

3. Results

3.1. Low-temperature sharp interfacial boundaries

Optimizing the electronic structure of high-aspect-ratio supercells can be challenging. Avoiding charge oscillations in the long-wavelength direction during band-by-band optimization can be difficult even using the iterative diagonalization methods. Results representative of the low-temperature sharp-interface limit for (100), (110) and (111) γ - γ' IFBs (i.e. pure *Ni* and stoichiometric *Ni₃Al*) are shown in Figs. 1 and 2. The interfacial energies are very sensitive to errors in the local spin moments. In order to illustrate the convergence of the electronic structure as a function of cell wavelength (λ) the total magnetic moment of the interfacial and *Ni* and *Ni₃Al* reference cells are shown in Fig. 1. As expected the supercell moment increases linearly with increasing λ and the increase in moment with cell size is the same for the defect and reference cells. Also the cells containing the IFB have a slightly smaller moment than the reference cells reflecting a slight decrease in the Ni moment near the IFBs. This observation is consistent with that reported by Price and Cooper using the full potential LMTO method [11].

Results for the sharp interfacial energies produced using strained *Ni* and *Ni₃Al* reference cells are shown in Fig. 2.

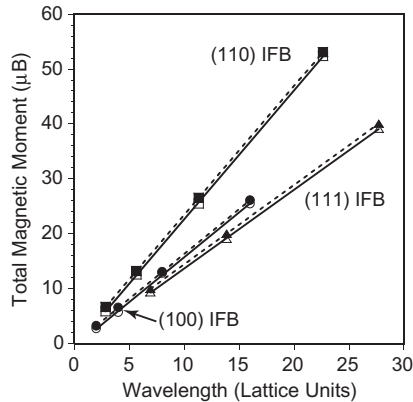


Fig. 1. Magnetic moments as a function of wavelength for supercells used to calculate the interfacial energies. Filled markers and dashed lines correspond to the supercells containing the IFBs and open markers and solid lines correspond to the reference cells for pure Ni and stoichiometric Ni_3Al . The latter magnetic moments are calculated by taking the average of Ni and Ni_3Al cells the same wavelength as the defect cell. As expected the moments scale with the length of the cells, and the interfacial and reference cells have nearly identical moments. The units for the length of the cells are taken as the periodic length in the (100), (110) and (111) directions: a_0 , $\sqrt{2}a_0$ and $\sqrt{3}a_0$, respectively, in lattice units.

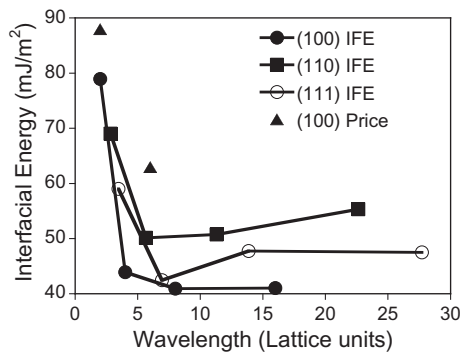


Fig. 2. The zero-temperature sharp interfacial energies as a function of wavelength for the (100), (110) and (111) $Ni-Ni_3Al$ IFBs (i.e. pure Ni and stoichiometric Ni_3Al). Previous full potential LMTO result of Price and Cooper for the (100) boundary are shown as open triangles [11]. The previous work did not include optimization of the atomic positions, which may explain the discrepancy with the current results. Convergence with cell size is more rapid along (100) and (110) as compared to (111).

Included in this figure are the previous results of Price and Cooper [11] for the (100) IFB. The current calculations include more degrees of freedom that are optimized during the relaxation process, so it is not surprising that the current (100) interfacial energies converge to a different value. The energies for the sharp (001), (110) and (111) IFBs converge to approximately 41, 55 and 48 $mJ m^{-2}$ respectively in the long-cell-wavelength limit.

3.2. Temperature-dependent results from Monte Carlo simulations

A cluster expansion (CE1) was developed for binary fcc structures in the Ni -rich portion of the phase diagram. This was constructed from 25 superstructures between the Ni fcc

and $L1_2$ endpoints, including 18 structures automatically generated by ATAT and seven additional superstructures (“special quasirandom structures” [29] and dilute impurities). All the reference calculations were run using ultrasoft pseudopotentials within the spin-polarized GGA approximation. The ATAT process produces a cluster expansion with seven pairs within ≈ 0.67 nm and two triplets within ≈ 0.36 nm with an overall cross-validation score of 0.008 eV. Here both configurational and vibrational entropic terms were assessed using techniques described previously. The resulting effective cluster interactions were then used to generate the Ni -rich part of the $Al-Ni$ phase diagram which is shown in Fig. 3. While the $\gamma + \gamma'$ two-phase region boundary is in good agreement with the experimental results of Zhang et al. (shown as a solid line) [30], the predicted $\gamma' + \gamma - \gamma$ boundary is higher than the experimental fit. At 15 at.% Al the predicted solvus line is ≈ 300 K higher than that interpolated from experiment.

It is worth noting that in a preliminary study effective cluster interactions were developed using the spin-averaged GGA approximation. The resulting phase diagram included the additional Ni_7Al phase anticipated by previous calculations based on spin-averaged LDA [12]. The phase lies in the middle of the composition range between γ and γ' and persists to temperatures above 600 K. As mentioned previously, to our knowledge, there is no experimental evidence that the Ni_7Al phase is stable in the binary $Ni-Al$ system.

3.3. Temperature-dependent interfacial boundary widths

The IFBs are simulated using high-aspect-ratio cells, where the periodic length normal to the IFB is at least twice

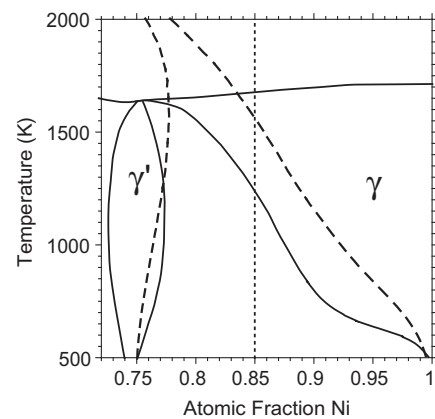


Fig. 3. The Ni -rich phase diagram produced by the first cluster expansion (CE1). Solid lines are from the CALPHAD calculations using the PANDAT method [30,40] and the dashed lines are cluster expansion predictions using Monte Carlo methods. For CE1 the ground state search, and the formation of the effective interaction coefficients, was initialized with the fcc endpoints Ni and $L1_2 Ni_3Al$. The $(\gamma + \gamma')/\gamma$ phase boundary is shifted to higher Ni compositions relative to experimental observations. At $Ni-15Al$ (at.%), represented in the figure as a vertical dotted line, the difference between the predicted and measured phase boundary is approximately 300 K.

the interface-plane periodic length. For example the (100) IFB was approximated with a cell with cubic lattice vectors of length $32 \times 32 \times 128$. The initial cell contained Ni and Ni_3Al slabs, of equal width, with a sharp (100) boundary aligned normal to the longest lattice vector (e.g the [001] direction). The cell was equilibrated at 1000 K using a two-step process. First, the cell composition had to be adjusted to reflect our target cell-composition of 15 at.% Al. This was accomplished by introducing a random distribution of Ni atoms on the Al sublattice in Ni_3Al . Next, this cell was equilibrated using a canonical ensemble Monte Carlo approach at this composition. After reaching equilibrium the Monte Carlo simulation is continued and snapshots of the IFB were collected at time intervals greater than 200 steps, ensuring uncorrelated measurements. For each measurement the concentration and long-range order (LRO) parameter are averaged over planes normal to the IFB. These profiles are then fit to a hyperbolic tangent, the individual profiles are shifted so that they share a common point of inflection and then all the data is binned normal to the IFB. The resulting curve is again fit to a general hyperbolic tangent function and the 10–90 width is taken from this fit. An example of the final (100) interfacial profile obtained by this procedure is shown in Fig. 4. Error bars on the data points represent one standard deviation and are obtained from averaging over 40 separate Monte Carlo snapshots. At 1000 K the interfacial 10–90 width is 2.06 ± 0.03 and 1.80 ± 0.03 nm for the composition and LRO parameter, respectively.

The (110) and (111) IFB widths were calculated using a similar procedure. The temperature dependence for the concentration and LRO parameter profiles of the three low-index boundaries are plotted in Figs. 5 and 6 respectively. At any given temperature the width of the (111) IFB is approximately 70% larger than the other boundaries. The rate of increase in interfacial width is approximately 0.21 nm for every 100 K for the (100) and (110) boundaries, with concentration and LRO having the same trends. The rate of change for the (111) boundary is slightly more rapid, 0.23 and 0.26 nm per 100 K for concentration and LRO, respectively. For a fixed composition, as the temperature approaches the solvus boundary, the Ni_3Al slab becomes thinner, making it more difficult to fit the boundary profiles. This is reflected in the poorer statistics found for the higher-temperature boundaries.

3.4. Interfacial excess free energy

One of the primary goals of this study is to estimate the γ - γ' interfacial excess free energy (IEFE). In order to accomplish this the following approach was used. For each low-index IFB two cells were constructed, with one cell having twice the length (λ) of the other normal to the respective IFBs. These cells were then equilibrated over a range of temperatures, typically from 10 to 1300 K, for an overall target composition of 15 at.% Al. At each temperature the equilibrated cells have the same volume

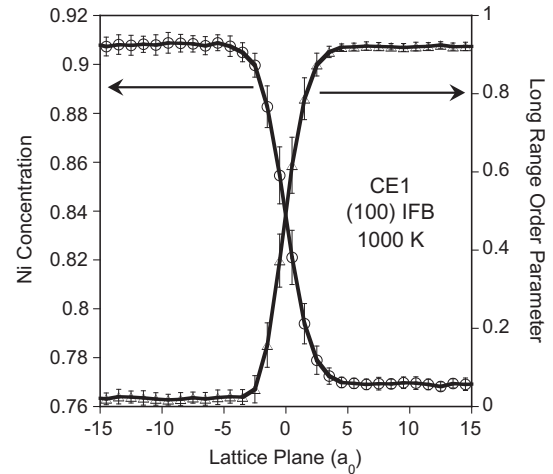


Fig. 4. The LRO and composition profile for the (100) γ - γ' IFB at 1000 K derived from Monte Carlo simulations using the first cluster expansion (CE1). Each data point in the profile is derived from 40 uncorrelated Monte Carlo snapshots of the IFB based on an overall cell composition of Ni-15Al (at.%). The profiles are centered about a common point of inflection, the data is then binned and averaged for each plane normal to the IFB. Each of the data points represent one of the (100) lattice planes, and includes error bars for the expected numerical error in the composition (i.e. one standard deviation).

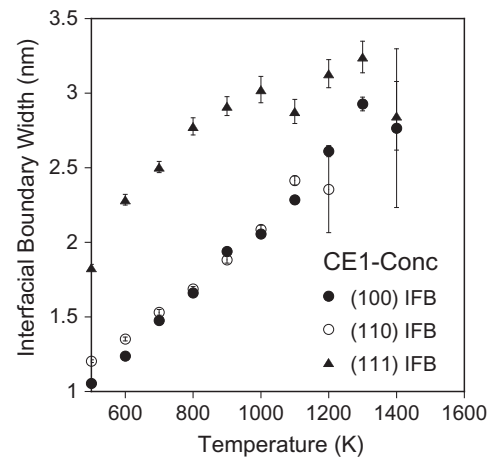


Fig. 5. The low-index, γ - γ' interfacial 10–90 widths, based on the composition profiles, as a function of temperature. The results are based on an overall cell composition of Ni-15Al (at.%) and CE1.

fraction of γ and γ' and the interfacial excess energy (IEE) is derived by subtracting the overall energy of the two cells ($2E_{\lambda/2} - E_{\lambda}$). Fig. 7 shows the IEFE as a function of temperature for the (100) IFB as calculated using cluster expansion CE1. The low-temperature boundary energies were calculated directly using a conventional sharp-interface model in the previous section. Comparing the predicted energies from these two techniques gives some indication of self-consistency between the cluster expansion and the conventional sharp-interface model. The cluster expansion, CE1, produces energies of 97, 94 and 40 mJ m^{-2} for the (100), (110) and (111) IFBs respectively. The values for the (100) and (110) IFBs are approximately

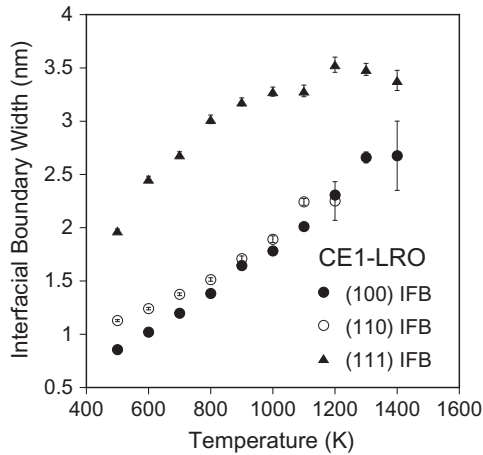


Fig. 6. The low-index γ - γ' interfacial 10–90 widths, based on the LRO parameter, as a function of temperature. The results are based on an overall cell composition of Ni–15Al (at.%) and CE1.

twice that found by directly calculating this energy using VASP (see Section 3.1) while the (111) energy is within 10 mJ m^{-2} . While these are substantial differences in energies at the low-temperature limit, it remains to be seen if the IEFE is strongly affected by this at higher temperatures. In order to assess this we derive the change in the IEFE with temperature and return to this issue by considering a second cluster expansion in the discussion section.

The IEFE is calculated by integrating the IEE over temperature using a generalization of the Gibbs–Helmholtz relation ($\partial F/T/\partial T = -E/T^2$, where F and E are the Helmholtz and internal energies, respectively):

$$IEFE(T) = E_0 - T \int_0^T \frac{IEE(T) - E_0}{T^2} dT. \quad (1)$$

The $IEE(T)$ is approximated by fitting the interfacial excess energy as a function of temperature at low temperature ($< 300 \text{ K}$) to $A + BT^4$, and at high temperatures ($> 300 \text{ K}$) to a fifth- or sixth-order polynomial in T . The resulting piecewise continuous function is numerically integrated using Eq. (1), yielding the IEFE as a function of temperature. An example of the excess energy variation

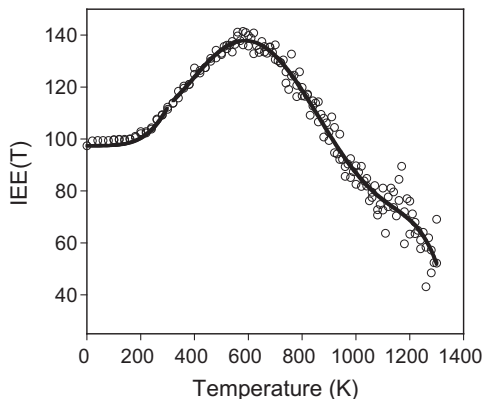


Fig. 7. The IEE as a function of temperature for the (100) γ - γ' boundary calculated using CE1. Open circles are the predicted energies, and the solid line is a piecewise continuous fit to the data.

with temperature and the fit to this function is shown in Fig. 7. The solid line is an example of a typical fit to the derived energies.

Fig. 8 shows the IEFE (i.e. Eq. (1)), derived using CE1, for the low-index boundaries at a nominal overall cell composition of 15 at.% Al. Note the rapid decrease in IEFE with increasing temperature. Comparing the predicted energies to that estimated from fits to coarsening experiments [8,10] we find very good agreement with experiment for the IEFES. The open circles in the figure are from fits to the coarsening data assuming that the free energy of mixing is ideal this reduces the interfacial free energy within the LSW model [8]. The two filled markers in the figure are results from the most recent fits to coarsening data. One of the data points was derived using the trans-interface-diffusion-controlled theory of coarsening which assumes that the rate-limiting process for coarsening is the diffusion rate through the diffuse (chemistry and LRO) IFB. Thus the filled circle and square are the result of fits to the same coarsening data using the classical LSW $t^{1/3}$ dependence and a $t^{1/2.42}$ dependence, respectively [10].

4. Discussion

4.1. Idealized low-temperature boundaries

The low-temperature sharp IFBs have been previously modeled using density functional theory by several groups. Price and Cooper [11] used the full potential LMTO method to explore the role of spin polarization on the stability of the (100) γ - γ' IFB. Using spin-averaged calculations on the (100) boundary yielded negative energies ranging from -23 to -118 mJ m^{-2} for $\lambda = 1$ and 3, a result not consistent with experimental observations. We have run similar calculations using GGA, with spin-averaged ultrasoft pseudopotentials, and find for a (100) IFB, with

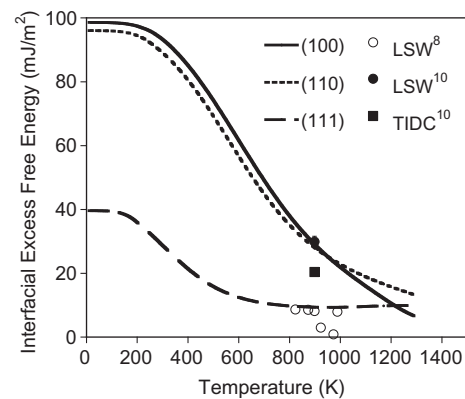


Fig. 8. The IEFE as a function of temperature for the (100), (110) and (111) γ - γ' boundaries calculated using CE1. The IEFE is derived by numerically integrating Eq. (1) using the piecewise continuous polynomial fit to the interfacial excess energy. The solid and dashed lines are the predicted IEFES which are in good agreement with energies derived from earlier coarsening experiments of Ardell. Open and filled circles are from coarsening data fit to LSW theory [8] and the filled square is from fits using trans-interface-diffusion-controlled theory [10].

$\lambda = 12$, an energy of -46 mJ m^{-2} . Proceeding with spin-polarized calculations on the same boundary, Price and Cooper found that the spin moments transitioned smoothly over 2–3 atomic layers, and identified this spin density transition across the boundary as the main contribution to the interfacial energy. The spin-polarized calculations yielded positive interfacial energies of $\approx 60 \text{ mJ m}^{-2}$ (see Fig. 2). We find a similar transition of spin density across all three low-index IFBs, and interfacial energies generally lower than the initial calculations of Price and Cooper. This is likely due to relaxing additional degrees of freedom over larger supercells (i.e. atomic positions and lattice parameters).

The low-temperature chemically sharp IFB energies for the (100), (110) and (111) are 41, 55 and 48 mJ m^{-2} respectively using density functional methods (ultrasoft pseudopotentials within S-GGA). Following Price and Cooper, the relative size of the interfacial energies is likely related to the degree to which the magnetic moment of Ni is disrupted by the introduction of the IFB along the three low-index directions. To a first-order approximation, the relative size of the interfacial energies reflects the number of atomic spin moments suppressed within a lattice constant on the Ni side the boundary.

More recently there has been one other first-principles study of the IFBs which focussed on tungsten segregation to the (100) γ - γ' interface, Amouyal et al. [31] used the local density approximation as implemented in VASP to calculate the low-index IFB energies. They report energies of the pure Ni/Ni_3Al interfaces of 42.6, 29.1 and 16.0 mJ m^{-2} for the (100), (110) and (111) interfaces, respectively. These are significantly lower than the converged values found in the current work.

4.2. Interfacial boundaries at high temperatures

Using the cluster expansion approach we find the IFBs at finite temperatures, as described through the composition and LRO parameter, change continuously across the boundary. As temperature increases the boundary broadens significantly. One interesting aspect of the interfacial widths is the consistently larger (111) IFB relative to the other low-index boundaries. First, this result is consistent with the low-temperature sharp interface results in that the (111) boundary converges at a significantly larger wavelength than the other two interfaces. Also, as pointed out by Ardell and Ozolins [9], the diffusion rates are expected to be 1–3 orders of magnitude times slower in the disordered Ni_3Al boundary than in disordered $Ni-Al$. Currently, the cuboidal structure of γ' precipitates often observed in the superalloys is attributed to the strain field produced by the lattice mismatch between the two phases. Combined with these observations, the current results imply that there may be a window of precipitate size, between the critical size and when the strain field dominates, where the kinetics would strongly favor precipitate growth along $\langle 100 \rangle$ and $\langle 110 \rangle$ as compared to $\langle 111 \rangle$.

The predictions for interfacial widths may prove useful in models of microstructure evolution that explicitly treat the transition between two domains (e.g. different phases, crystal orientation) using a regular grid of sampling points. Given the predicted changes in interfacial widths with temperature it is likely that incorporating these effects will be important when modeling non-isothermal processes. For Ni-based superalloys, solution heat-treatments and in-service temperatures can range from 900 to 1625 K. This corresponds to a change in predicted boundary width of 1.2 nm, in some cases doubling the width of the boundary. In order for models using a regular grid to satisfy Nyquist's theorem at least two grid points should fall within the boundary. This requirement effectively limits the scale of such calculations to the processing limitations of available computer hardware. For example, in the low-temperature limit grid spacing should be less than $\approx 0.5 \text{ nm}$ to model the (110) and (111) concentration profile in γ - γ' . Assuming a practical upper limit on the fast Fourier transform (FFT) grid of 512^3 , such methods applied to this material are limited to volumes of less than a cube with edge length of $\approx 0.25 \mu\text{m}$ at 900 K. It is not unusual to find γ' particles larger than $1 \mu\text{m}^3$ in engineering alloys and this could limit the use of FFT-based microstructural evolution codes in this class of problems.

Recent advances in electron optics have enabled a much more detailed characterization of the IFB. There have been several recent studies employing high-resolution scanning transmission electron microscopy (HRSTEM) with atomic-resolution Z contrast imaging (e.g. high-angle annular dark-field; HAADF). Srinivasan et al. [32] characterized a (100) γ - γ' IFB in the Ni-based superalloy Rene 88DT that had been annealed at 1039 K for 50 h. By aligning the sample along $\langle 010 \rangle$ columns of atoms can be identified, using image intensity and contrast, that correspond to the γ and γ' phases. Using just this information the position and width of the boundaries was estimated as 2.7 and 1.3 nm for the concentration and LRO parameter, respectively. In order to assess the compatibility of this approach with the techniques used in this paper we have applied a similar intensity and contrast method based on the concentration of Ni along atomic columns adjacent to a (100) interface, oriented as described above. We find that the two methods produce similar IFB widths that, for the cases tested, were within statistical error. While the predicted interfacial widths are within the range measured in the superalloy Rene 88DT, the current calculations generally predict the LRO and composition interfacial widths to be approximately equal over a wide range in temperature.

The HRSTEM-HAADF characterization also showed that the midpoint (i.e. point of inflection) of the composition and LRO profiles are offset by approximately 0.6 nm, with the LRO midpoint closer to the γ side of the boundary [32]. This is a particularly interesting observation, because it allows the system to stabilize shells of material around γ' particles that do not share the ordering or chemistry of either of the equilibrium phases. Current

Monte Carlo simulations of the (100) and (110) boundaries based on the cluster expansion (CE1) exhibit a small shift, $\delta_{C-LRO} = \langle \text{arcTanh}(0)_C \rangle - \langle \text{arcTanh}(0)_{LRO} \rangle$, which reaches a maximum of ≈ -0.1 nm at 700 K. However, the (111) boundary produces a positive shift that increases to almost 0.4 nm at higher temperatures, though the error in this value also increases with temperature as shown in Fig. 9. Hence, even using a relatively simple binary cluster expansion to compute via the Monte Carlo method the entropic contributions to the interfacial width can represent the variation in behavior found in complex alloys such as Rene 88DT.

A second more recent study by Ge et al. [33] performed similar HAADF imaging of a (100) boundary in a second-generation Ni-based superalloy (DD6). This particular alloy contains 2 wt.% Re, an element not present in Rene-88DT, which is known to improve high-temperature creep performance in this class of alloys. The DD6 sample had a final anneal at 1143 K for 32 h. The HAADF images of an (100) IFB were analyzed using image intensity and contrast to identify the concentration and LRO profiles across the interface. In this case the interfacial widths was found to be approximately 2.2 nm for both concentration and LRO parameter, and in contrast to earlier work on Rene 88DT there is no apparent shift in the point of inflection of the two profiles. Perhaps fortuitously, at these annealing temperatures the measured width is in good agreement with the predicted widths for the (100) and (110) IFBs for Ni–Ni₃Al.

More recently Plotnikov et al. [34] have used 3-D atom probe tomography to characterize γ' particles in binary Ni–Al alloys. This study focused on the evolution of particle size and IFB width of during annealing at two temperatures (823 and 873 K) for times ranging from 5 min to 4096 h. The IFB widths were determined using a spline fit to the proximity histogram of the composition profile. The 10–90 width was determined for profiles at two

compositions, Ni–12.5Al and Ni–13.5Al. For the former composition aged at 873 K for 256 h the measured interfacial width is approximately 1.6 nm; this in good agreement with the predicted values for Ni–15Al at this temperature. It is worth noting that capillary effects on the chemistry of aged submicron precipitates are likely to produce Ni-rich γ' compared to the slabs used in the current calculations. However, the interfacial width is weakly dependent on the Al content as shown in the atom probe study [34].

4.3. Interfacial excess free energies

The IEFEs calculated using CE1 drop precipitously with increasing temperature. As shown in Fig. 8, predicted values at high temperature fall within the range of the limited measurements based on growth kinetics. These calculations have also been performed with and without the vibrational and electronic entropic contributions using techniques described previously in the literature [14]. Surprisingly, we find that the free energy of the diffuse interfaces is dominated by the configurational entropy. Recently Mao et al. [35] estimated the vibrational entropic contributions to the free energy of sharp (100), (110) and (111) γ – γ' interfaces in Ni–Ni₃Al using the harmonic approximation. They found that there are significant vibrational energy contributions to the free energy for the sharp, ordered IFBs. The discrepancy between these two results is likely due to the differences in vibrational entropy of the high-temperature boundary as represented in the ordered and disordered limits. Previously, van de Walle et al. [36] have shown that changes in vibrational entropy between ordered and disordered Ni₃Al is small over a wide temperature range. In the current study, as the temperature rises the IFB becomes disordered and diffuse, so changes in the vibrational entropy contributions will be small. If the boundary remains ordered, as the temperature increases, changes in the vibrational entropy may begin to dominate the entropic contributions to the free energy. These results, taken with the insights from the previous work of Mao et al. on sharp interfaces, may help explain trends in free energies as groups begin exploring the effects of more complex chemistries on the energies of these interfaces.

The initial cluster expansion of the Ni–Al system provides an adequate approximation of the Ni-rich phase diagram and the width of the IFBs at elevated temperatures. However, this cluster expansion does not produce energies consistent with the low-temperature sharp-interfacial energies found using explicit density functional calculations as described in Section 3.1. In order to determine if this has a significant effect on the IEFIE or its temperature dependence, a second cluster expansion was considered.

The second cluster expansion (CE2) was developed by adding to the set of input structures the three shortest-wavelength IFBs calculated previously (see Section 3.1). The intent was to bias the expansion to maintain a more precise representation of the low-temperature IFB energy.

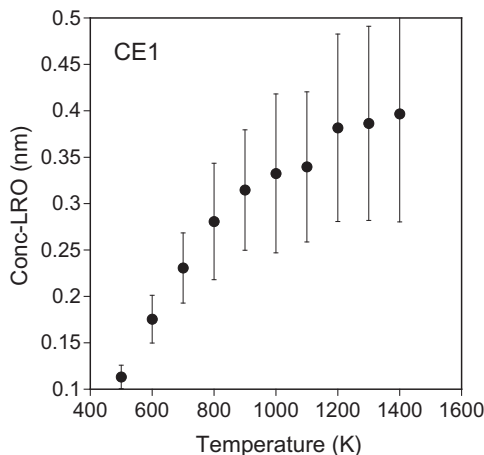


Fig. 9. The shift in the point of inflection (δ_{C-LRO}) for the concentration and LRO profiles of the (111) γ – γ' IFB. Results are based on an overall cell composition of Ni–15Al (at.%) and CE1.

Within the ATAT process this produced four pairs within ≈ 0.5 nm, and a triplet and quartet within ≈ 0.25 nm with a cross-validation score of 0.008 eV. The resulting effective cluster interactions were then used to generate the Ni-rich part of the Al–Ni phase diagram based as shown in Fig. 10. Here the two-phase region is narrowed significantly, with the $\gamma'/(\gamma' + \gamma)$ boundary moving to higher Ni concentrations and the high-temperature portion of the $(\gamma' + \gamma)/\gamma$ boundary moving to slightly lower Ni concentrations relative to the first cluster expansion. Evaluating the low-temperature sharp interfacial energy using this cluster expansion produces energies of 42, 46 and 39 mJ m^{-2} for the (100), (110), and (111) boundaries, respectively. This is in much better agreement with energies calculated directly from VASP (Section 3.1), 41, 55 and 48 mJ m^{-2} for the (100), (110) and (111) boundaries, respectively.

Fig. 11 shows the results of integrating interfacial excess energy (Eq. (1)) produced with CE2 for the three low-index boundaries in order to produce the IEFE. As shown in the figure these energies drop rapidly with increasing temperature, becoming constant and fall in a narrow energy range (9–12 mJ m^{-2}) for temperatures above 600 K. The second cluster expansion produces an average IEFE of approximately 11 mJ m^{-2} for the three low-index boundaries, which is very good agreement with LSW analysis published in the mid-1990s [8].

The two cluster expansions exhibit a rapid decrease in the IEFE with temperature, with CE2 producing a narrow window of the three free energies over most of the temperature distribution. At high temperatures, above 1000 K, the two approximations give similar results but with different slopes for the (110) and (110) IEFEs. Because of the slow

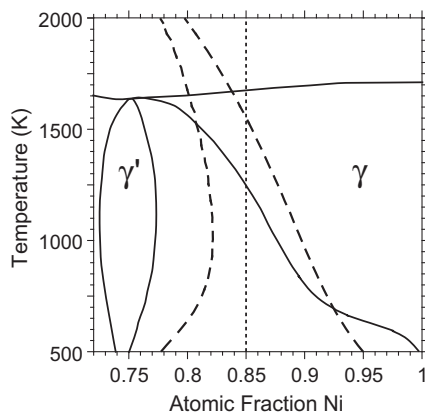


Fig. 10. The Ni-rich phase diagram produced by the second cluster expansion (CE2). Solid lines are from CALPHAD calculations using the PANDAT method [30,40] and the dashed lines are cluster expansion predictions using Monte Carlo methods. By initializing the ground state search within ATAT using fcc Ni, L_{12} Ni₃Al and the relaxed (100), (110) and (111) IFBs the $\gamma'/(\gamma' + \gamma)$ phase boundary is shifted to higher Ni compositions relative to CE1. The $(\gamma + \gamma')/\gamma$ phase boundary remains relatively unchanged compared to CE1. The vertical dotted line in the figure marks the Ni–15Al (at.%) composition.

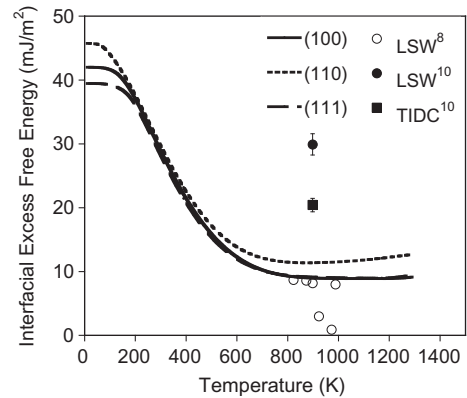


Fig. 11. The IEFE as a function of temperature for the (100), (110) and (111) γ – γ' boundaries calculated using CE2. The IEFE is derived by numerically integrating Eq. (1) using the piecewise continuous polynomial fit to the IEFE. The solid and dashed lines are the predicted IEFEs, and are in good agreement with IEFEs derived from earlier coarsening experiments of Ardell. Open and filled circles are from coarsening data fit to LSW theory [8] and the filled square is from fits using trans-interface-diffusion-controlled theory [10].

kinetics of these alloy systems microstructural evolution simulations would typically be in the range of 800–1450 K.

Given the key role the γ' particles play in the high-temperature strength of Ni-based superalloys it is worth speculating on mechanisms that could stabilize the precipitates to higher temperatures. As the temperature rises the configurational entropy in Ni increases which acts to reduce the IEFE. Given the strong evidence of the role of the local magnetic moment of Ni in increasing the IFB energy it is reasonable to assume that introducing atomic species with strong local magnetic moments, that preferentially favor the γ phase, could stabilize the IFB to higher temperatures.

5. Summary

First-principles methods were used to assess the structure, energies and free energies of low-index γ – γ' boundaries in the Ni–Ni₃Al system. We verify the previous work of Price and Cooper that within the GGA approximation these IFB energies are positive only when one includes the spin degrees of freedom. The relative energies of the low-temperature chemically sharp IFBs reflect the number of Ni spin moments that are suppressed by the introduction of the interface. This effect appears to be relatively short range for the (100) and (110) IFBs and longer range for the (111) boundary. However, to a first-order approximation the largest contribution to the energy is due to the spin suppression in the first all-Ni layer adjacent to the boundary.

Spin-polarized Ni–Al reference configurations are also needed when developing effective cluster interaction coefficients for use in a cluster expansion description of the Ni-rich portion of the binary phase diagram. Cluster expansions based on spin-averaged calculations produce at least

one unexpected phase (Ni_7Al) in the Ni-rich portion of the binary phase diagram that is stable at high temperatures. This result is consistent with the previous density functional calculations by Wolverton and Zunger [12], who found that magnetization destabilizes the Ni_7Al phase relative to Ni and Ni_3Al .

Using a simple cluster expansion in conjunction with Monte Carlo methods we find the widths of the low-index IFBs in the range of 1.0–3.0 nm depending on the boundary and the temperature. The width of the (111) IFB is generally ≈ 1.7 times larger than the (100) and (110) boundaries at any given temperature. The rate of increase in width as a function of temperature ranges from 0.2 to 0.3 nm per 100 K. Given the relatively narrow IFB widths we conclude that phase evolution methods that explicitly model the boundaries will be limited to relatively small simulation volumes. This approach also predicts a small, temperature-dependent, shift in the centers of the boundaries as defined through the concentration and LRO parameter. The shift is smaller than that observed in Rene 88DT using high-resolution TEM imaging methods [32].

The IEFEs are also strongly temperature dependent, falling to $\approx 10 \text{ mJ m}^{-2}$ at 1000 K. The largest entropic contributions to the free energy are from the configurational degrees of freedom while the vibrational and electronic terms are smaller for the disordered IFBs. The IEFE has been studied using two different cluster expansions and the general trends are insensitive to the specifics of ECIs. The results for the binary Ni–Al system are encouraging. Given the chemical complexity of commercial Ni-based superalloys studies of the effects of high concentrations of ternary elements (e.g. Cr or Co) on the IFBs would be highly desirable.

Acknowledgements

This research was supported in part by grants from the Air Force Research Laboratory, Materials and Manufacturing Directorate (F33615-01-C-5214), the Air Force Office of Scientific Research (2306AL3P), and computer time from the DoD High Performance Computing Modernization Program at the Air Force Research Laboratory DoD Supercomputing Research Center (AFRL-DSRC). The authors gratefully acknowledge insightful discussions with Profs. J. Perdew, Zi-Kui Liu, Yungzi Wang, and Barry Cooper over the course of this project. One of the authors (C.W.) is particularly grateful for initial discussions in the mid-1990s with David Price about his work in this area.

References

- [1] Lifshitz IM, Slyozov V. *J Phys Chem Sol* 1962;19:35.
- [2] Wagner C. *Z Elektrochem* 1961;65:581.
- [3] Ardell AJ. *Acta Metall* 1968;16:511.
- [4] Chellman DJ, Ardell AJ. *Acta Metall Mater* 1974;22:577.
- [5] Wendt H, Haasen P. *Acta Metall Mater* 1983;31:1649.
- [6] Xiao SQ, Haasen P. *Acta Metall Mater* 1991;39:651.
- [7] Calderon HA, Voorhees PW, Murray JL, Kostorz G. *Acta Metall Mater* 1994;42:991.
- [8] Ardell AJ. *Interface Sci* 1995;3:119.
- [9] Ardell AJ, Ozolins V. *Nature Mater* 2005;4:309.
- [10] Ardell AJ. *J Mater Sci* 2011;46:4832.
- [11] Price DL, Cooper BR. *Materials theory, simulations, and parallel algorithms*, vol. 408. Materials Research Society; 1996. p. 463–8.
- [12] Wolverton C, Zunger A. *Phys Rev B* 1999;59:12165.
- [13] Schonfeld B, Reinhard L, Kostorz G, Bührer W. *Acta Mater* 1997;45:5187.
- [14] van de Walle A, Ceder G. *J Phase Equilib* 2002;23:348. <http://dx.doi.org/10.1361/105497102770331596>.
- [15] van de Walle A, Asta M. *Model Simul Mater Sci Eng* 2002;10:521.
- [16] Kresse G, Joubert D. *Phys Rev B* 1999;59:1758.
- [17] Vanderbilt D. *Phys Rev B* 1990;41:7892.
- [18] Blöchl PE. *Phys Rev B* 1994;50:17953.
- [19] Perdew JP. In: Ziesche P, Eschrig H, editors. *Electronic structure of solids '91*. Berlin: Akademie Verlag; 1991. p. 11–20.
- [20] Vosko SH, Wilk L, Nusair M. *Can J Phys* 1980;58:1200.
- [21] Glueckstein JC, Klebanoff LE. *Phys Rev B* 2003;68:052407.
- [22] Idzikowski B, Kudryavtsev Y, Hyun YH, Lee YP, Klenke J. *J Alloy Compd* 2006;423:267.
- [23] Sanchez JM, Ducastelle F, Gratias D. *Physica* 1984;128A:334.
- [24] de Fontaine D. *Solid State Phys* 1994;47:33.
- [25] Zunger A. In: Turchi PE, Gonis A, editors. *NATO ASI on statics and dynamics of alloy phase transformation*, vol. 319. New York: Plenum Press; 1994. p. 361.
- [26] Ducastelle F. *Order and phase stability in alloys*. New York: Elsevier Science; 1991.
- [27] van de Walle A, Asta M, Ceder G. *CALPHAD J* 2002;26:539.
- [28] van de Walle A. *Calphad J* 2009;33:266.
- [29] Zunger A, Wei SH, Ferreira LG, Bernard JE. *Phys Rev Lett* 1990;65:353.
- [30] Zhang F, Chang Y, Chen SL, Oates W. *Acta Mater* 2003;51:207.
- [31] Amoyal Y, Mao Z, Seidman DN. *App Phys Lett* 2008;93:201905.
- [32] Srinivasan R, Banerjee R, Hwang J, Viswanathan G, Tiley J, Dimiduk D, et al. *Phys Rev Lett* 2009;102:086101.
- [33] Ge B, Luo Y, Li J, Tang D, Gui Z. *Philos Mag Let* 2012;92:541.
- [34] Plotnikov E, Mao Z, Noebe R, Seidman D. *Scr Mater* 2014;70:51.
- [35] Mao Z, Booth-Morrison C, Plotnikov E, Seidman D. *J Mater Sci* 2012;47:7653.
- [36] van de Walle A, Ceder G, Waghmare UV. *Phys Rev Lett* 1998;80:4911.
- [37] Simmons G, Wang H. *Single, crystal elastic constants*. Cambridge, MA: MIT Press; 1971.
- [38] Prikhodko S, Carnes J, Isaak D, Yang H, Ardell A. *Met Mat Trans A* 1999;30A:2403.
- [39] Pearson WB. *A handbook of lattice spacings and structures of metals and alloys*. NY: Pergamon Press; 1967.
- [40] Cao W, Chen SL, Zhang F, Wu K, Yang Y, Chang Y, et al. *Calphad* 2009;33:328.